Dalton Transactions

ROYAL SOCIETY OF CHEMISTRY

PAPER

View Article Online
View Journal | View Issue

Cite this: *Dalton Trans.*, 2026, **55**, 1716

Photoactive Fe(III) pyclen complexes for light-driven aerobic oxidation of *p*-xylene

Matteo Alberti,[a] Greta Rossi,[b] Djihed Boucherabine,[a] Fausto Cargnoni, *[c] Mario Italo Trioni,[c] Giulia Taini,[a] Dominika Zakutna,[d] Arianna Gentilin,[b] Luka Đorđević,[b] Andrea Sartorel *[b] and Alessandro Caselli *[a,c]

Iron complexes have drawn attention for decades as biomimetic models of enzyme active sites that promote oxidative transformations. Many reports indeed deal with catalytic systems where iron complexes catalyze the oxidation of organic compounds exploiting chemical oxidants, including dioxygen, through thermal activation. Conversely, reports where the photochemical activation of iron complexes is proven are less frequent. In this work, we describe the photochemical activation of iron(III) pyclen complexes, [Fe(III)(X)$_2$pyclen]X (pyclen = 3,6,9-triaza-1(2,6)-pyridinacyclodecaphane; X = Cl, Br, OTf, **1a–c**; OTf = triflate, $CF_3SO_3^-$), and their application to the aerobic oxidation of *p*-xylene under visible light (up to 415 nm). Complexes **1a–c** have been synthesized and characterized, combining structural analysis, Mössbauer spectroscopy, and magnetization. Notably, spectroscopic UV-Vis analyses combined with DFT and TD-DFT calculations show that they have extended absorption up to the visible region attributed to (pyclen/X) ligand-to-metal transitions and that the absorption of light may induce a homolytic cleavage of the Fe–X bond. The nature of X impacts the photochemical activity of the iron complexes towards the oxidation of *p*-xylene under visible light, with **1b** (X = Br) leading to the privileged formation of *p*-tolualdehyde, while **1a** (X = Cl) and **1c** (X = OTf) are almost inactive. The reactivity of **1b** is rationalized by the photochemical generation of bromine radicals (Br$^\bullet$) as the active species operating through a hydrogen atom transfer (HAT) reaction towards *p*-xylene, as supported by the Bond Dissociation Free Energies (BDFEs) of H–Br (BDFE = 87 kcal mol^{-1}) and the C–H bond in *p*-xylene (BDFE = 80 kcal mol^{-1}). Kinetic and EPR evidence supports a radical autooxidation pathway. This work will guide new studies on the photochemical reactivity of iron complexes towards light-driven, sustainable organic oxidation processes.

Received 22nd October 2025,
Accepted 11th December 2025

DOI: 10.1039/d5dt02534f

rsc.li/dalton

Introduction

The selective oxidation of hydrocarbons plays a crucial role in industrial synthesis and academic research.[1] Despite recent efforts to use more sustainable routes, industrial oxidation processes heavily rely on highly toxic metal-oxo reagents (*e.g.*, $KMnO_4$) and metal oxide surfaces.[2] Although progress in developing more sustainable processes has been reported in recent decades,[3] the demand for selective, efficient, and eco-friendly oxidation methods continues to grow.

The use of iron[4] – the most abundant transition metal on Earth – and its complexes has attracted considerable interest in oxidation catalysis for organic synthesis, biochemistry, and industrial applications.[5] Significant advancements in this field over recent years have been highlighted in several comprehensive reviews.[6–16] Natural mononuclear nonheme iron enzymes are pivotal in essential oxidative transformations, efficiently catalysing a wide range of chemical reactions.[17,18] Efforts to develop synthetic models that replicate Nature's strategies continue to be a highly active research area.[19–25] In both these enzymes and their synthetic counterparts, high-valent iron-oxo intermediates, such as iron(III)-superoxo, iron(III)-peroxo, iron(III)-hydroperoxo, and iron(IV)- or iron(V)-oxo species, play a central role.[17,26]

Iron(III)-superoxo species have been identified as active species in C–H bond activation and oxygen atom transfer (OAT) reactions.[27] However, their activity is largely limited to weak, activated C–H bonds. In contrast, the reactivity of nonheme iron(III)-hydroperoxo species remains a topic of debate and is the subject of extensive experimental and theore-

[a]*Department of Chemistry, Università degli Studi di Milano, Via Golgi, 19, 20133 Milano, Italy. E-mail: alessandro.caselli@unimi.it*
[b]*Department of Chemical Sciences, University of Padova, via Marzolo 1, 35131 Padova, Italy. E-mail: andrea.sartorel@unipd.it*
[c]*Istituto di Scienze e Tecnologie Chimiche "G. Natta" CNR-SCITEC, via Golgi 19, 20133 Milano, Italy. E-mail: fausto.cargnoni@scitec.cnr.it*
[d]*Department of Inorganic Chemistry, Charles University, Hlavova 2030/8, 128 40, Prague 2, Czech Republic*

tical investigations.[28] Meanwhile, nonheme iron(IV)-oxo species are established as competent oxidants, capable of abstracting hydrogen atoms in C–H bond activation reactions.[23]

Among nonheme catalysts, iron complexes with polyamine and aminopyridine ligands occupy a prominent position.[29,30] Notably, iron(II) complexes of tetradentate N4 donor ligands, such as $[Fe(CF_3SO_3)_2(pyclen\text{-}Me_3)]$ (pyclen = 3,6,9-triaza-1(2,6)-pyridinacyclodecaphane; $CF_3SO_3^-$ is the triflate anion, hereafter abbreviated OTf^-), are readily oxidized by H_2O_2 to form a hydroperoxo iron(III) species.[31,32] This species, following acid-triggered O–O bond cleavage, becomes active in the stereospecific hydroxylation of strong C–H bonds.[33]

Our group has focused on the synthesis and coordination behavior of pyridine-based 12-membered tetraaza-macrocyclic ligands.[34,35] We described the synthesis and characterization of robust $[Fe(III)X_2(pyclen)]^+$ complexes, which are highly active and selective for alkene oxidation using hydrogen peroxide as the terminal oxidant, without the need for additives (Fig. 1a).[36] It is noteworthy that depending on the anion (X^-) of the iron (III) complex used as the catalyst, we observed selective formation of epoxide (X = Cl) or a clean dihydroxylation reaction (X = OTf). Intrigued by these results, we further explored the reactivity of iron(III) pyclen complexes in the selective oxidation of alcohols using H_2O_2, without any acid co-catalyst (Fig. 1b).[37] Hydrogen peroxide is an appealing oxidant since the only by-product is water; however, the ideal oxidant is surely molecular oxygen, O_2, which can address sustainability priorities in industry.[38] In this context, the combined use of visible light and dioxygen for the photocatalytic oxidation of hydrocarbons offers an atom-economical and greener alternative to traditional methods.[39,40]

While iron complexes have been extensively investigated in the chemical activation of oxidants, their reactivity with light towards photocatalytic processes remains less explored.[41] They have attracted particular interest since the recent renaissance of photocatalysis towards sustainable processes and synthetic organic chemistry, with solar reforming being indeed an emerging technology for circular chemical industries.[42] Recent examples dealt with FeX_3 (X = Cl, Br) photochemical reactivity towards upcycling of polystyrene, *via* photochemical generation of X˙ radicals (Fig. 1c).[43,44]

Inspired by our findings and the assessed photochemical reactivity of FeX_3,[45] we aimed to investigate iron(III)(pyclen) complexes bearing halide or pseudo-halide ligands as photochemically active species for the generation of radicals. We report here that Fe(III) pyclen complexes are indeed competent catalysts for the aerobic catalytic oxidation of *p*-xylene induced by visible light, without needing any additive. In particular, $[Fe(III)X_2(pyclen)]^+$ complexes, with chloride, bromide, and triflate ligands (**1a**, **1b**, and **1c**, respectively), were synthesized and fully characterized, combining structural analysis, Mössbauer

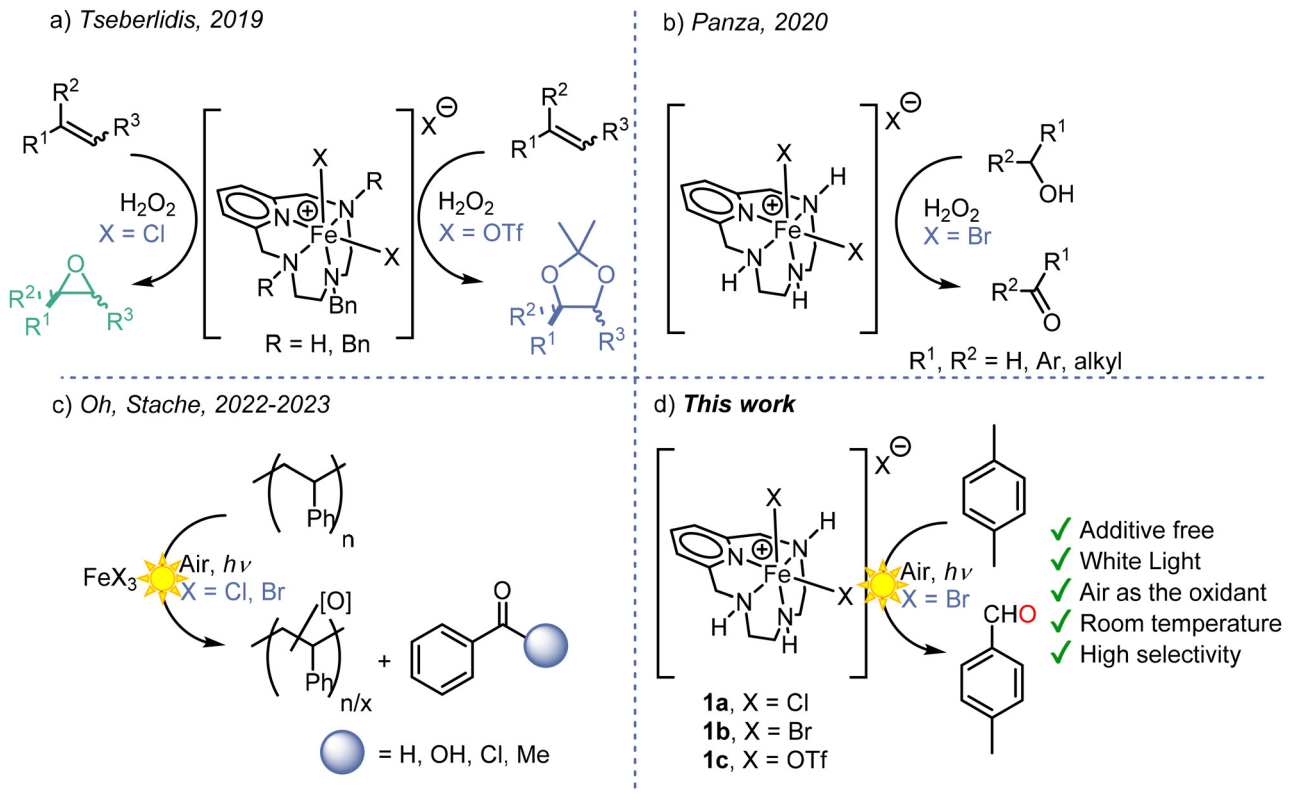

Fig. 1 (a and b) Oxidation reactions catalysed by $[Fe(III)(X)_2pyclen]X$ complexes using H_2O_2 as the terminal oxidant; (c) photochemical valorisation of polystyrene with FeX_3 (X = Cl, Br); (d) selective light-induced (white light or 405 nm LED) aerobic oxidation of *p*-xylene reported in this work.

spectroscopy, and magnetization. UV-Vis spectroscopic analysis shows that the iron complexes have extended absorption up to the visible region, and TD-DFT calculations predict that these absorption features are due to (pyclen/X) ligand-to-metal transitions and that the absorption of light may induce a homolytic cleavage of the Fe–X bond. Consistently, the Fe(III) pyclen complex **1b** carrying a bromide ligand is active in the oxidation of *p*-xylene to yield *p*-tolualdehyde (Fig. 1d), operating through a photoinduced radical chain mechanism.

Results and discussion

Synthesis and characterization of Fe(III) pyclen complexes

Complexes **1a–c** were obtained by treating pyclen with the appropriate iron(III) salt precursor (Scheme 1). In the case of complexes **1a** and **1b**, they were recovered from the reaction medium as precipitates in high yield and purity. Conversely, the higher solubility of the triflate complex, **1c**, rendered its collection more complicated, and any attempt to precipitate the complex from acetonitrile met with failure. The product was then collected by evaporation of the solvent as a deep yellow oil in quantitative yield and then treated with cold diethyl ether to obtain a brownish precipitate. Nonetheless, HR-MS analysis confirmed the expected formation of the complex.

Several crystal structures of $[FeX_2(pyclen)]^+$ cationic complexes, balanced with various counterions, have been reported.[37,46–50] Interestingly, crystallization of compound **1a** *via* solvent diffusion (methanol/diethyl ether, v/v = 1 : 2) led to the concomitant precipitation of two distinct crystal morphologies: clear, yellow, regular blocks (**1a**) and elongated, dark brown plates (**1a′**). While structural analysis of the former matched previously published work by Green and co-workers (CCDC 1578766),[49] featuring a chloride counterion, the latter displayed a novel structure, which was determined *via* X-ray diffraction (Fig. S1–S4 and Tables S1–S7 in the SI, including a detailed comparison of the X-ray structural features of compound **1a′** with analogous structures published in the Cambridge Crystallographic Data Centre, including **1a** and **1b**). X-ray diffraction analysis of **1a′** revealed that although it shares the same molecular geometry and *cis*-folded tetraaza-macrocycle configuration as **1a**, it incorporates a divalent $[Fe(II)Cl_4]^{2-}$ anion in its second coordination sphere. The presence of $[MCl_4]^{n-}$ species as counterions in analogous cationic coordination compounds has been previously observed by our group[36] and others.[49,51] Auto reduction of Fe(III) to Fe(II) accompanied by oxidation of the halide with concomitant release of X_2 gas has been previously reported.[52]

In all these structures, the Fe(III) center adopts a distorted octahedral geometry, coordinated by the four nitrogen atoms of the macrocycle and two monodentate X-type ligands. The pyclen scaffold displays a *cis*-folded conformation, which has been demonstrated by molecular mechanics calculations to be preferred when M–N bond lengths are greater than 2.0 Å.[53]

We gained further insight into the structural distortion of these complexes with respect to an ideal octahedral arrangement by comparing experimental structures with those computed for the gas phase and solvated states of **1a** and **1b**. Interestingly, the crystalline structures are in better agreement with data extracted from solvated complexes than from gas-phase ones, as detailed in Tables S4 and S11 of the SI section. Indeed, for both **1a** and **1b**, the relevant geometrical parameters of gas-phase molecules differ from the experimental crystalline values by almost 0.05 to 0.1 Å, while the inclusion of solvation effects in the computations reduces these discrepancies by more than half. This outcome suggests that the dissolution of **1a**, **1b**, and **1c** in a solvent with medium polarity partially mimics crystal field effects. This analysis, although limited to geometrical features, supports a proper description of the systems under investigation by the employed computational approach.

To elucidate the oxidation state of the iron complexes, Mössbauer spectroscopy was performed on solid-state samples at room temperature using nitrogen-flushed sample holders. Fitting results are summarized in Table S8, with a qualitative analysis provided in the SI. As expected, complex **1a** exhibits a high-spin Fe^{3+} center (see Fig. S5, left). In contrast, complexes **1b** and **1c** display signatures of Fe^{2+}. For **1b**, this likely arises from partial reduction of $FeBr_3$ to $FeBr_2$ under vacuum and heating conditions (Fig. S5, right). In the case of **1c**, however, the Fe^{2+} signal originates from impurities in the commercial $Fe(OTf)_3$ precursor, which Mössbauer analysis revealed to contain up to 46% Fe^{2+} (Table S9). To resolve this, we syn-

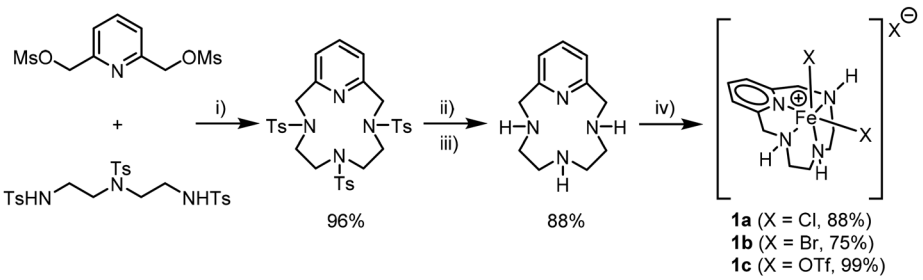

Scheme 1 Synthetic route used to obtain ferric complexes **1a–c**. (i) K_2CO_3, CH_3CN, reflux; (ii) H_2SO_4 conc., microwave; (iii) NaOH; (iv) FeX_3, CH_3CN, Δ. Commercially available iron(III) trifluoromethanesulfonate may be heavily contaminated with iron(II) species (up to 43%; see the SI and Table S9). Therefore, we synthesized an $Fe(III)(OTf)_3$ precursor in-house from ferric chloride to avoid any trace of Fe(II), as detailed in the SI.

thesized in-house pure $Fe(OTf)_3$ starting from pure anhydrous $FeCl_3$, and when complex **1c** was prepared with this iron(III) triflate source, Mössbauer spectroscopy did not show any evident sign of the presence of Fe^{2+} (Fig. S6, right).

The spin states of complexes **1a** and **1b** were further assessed using macroscopic magnetization measurements. Zero Field Cooled (ZFC) and Field Cooled (FC) magnetization curves were recorded at 0.5 T, and in both samples, they overlapped completely. The temperature dependence of the molar magnetic susceptibility-temperature product ($\chi_M T$) for complexes **1a** and **1b** is presented in Fig. 2. For complex **1a** (Fig. 2a), deviation from the ideal Curie or Curie–Weiss (represented by the teal dashed line in Fig. 2a) behavior at low and high temperatures indicates antiferromagnetic interactions and zero-field splitting. These effects were modelled using the modified Van Vleck approach.[54] The result, which incorporates both zero-field splitting and axial distortion, yielded an excellent fit (Fig. 2a, magenta line). The fit parameters are summarized in Table 1, while the equation, derived for this system, is as follows:

$$\chi = \frac{\chi_z + 2\chi_x}{3}$$

$$\chi_z = \frac{N{g_z}^2{\mu_B}^2}{4k(T-\theta)} \cdot \frac{1 + 9e^{-\frac{2D}{k(T-\theta)}} + 25e^{\frac{-6D}{k(T-\theta)}}}{1 + e^{-\frac{2D}{k(T-\theta)}} + e^{-\frac{6D}{k(T-\theta)}}}$$

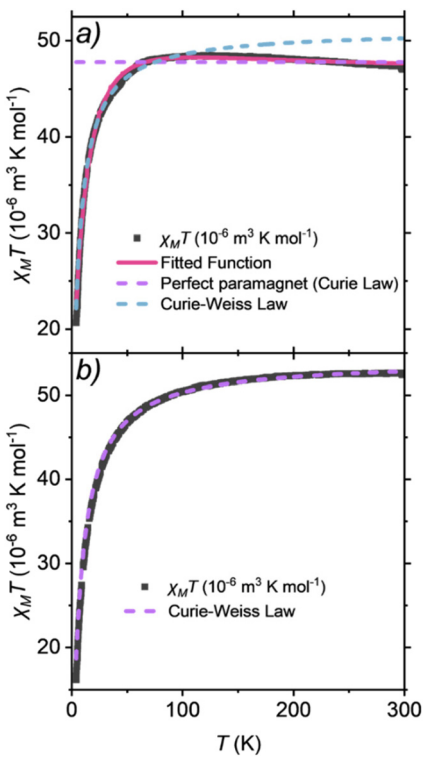

Fig. 2 $\chi_M T$ product as a function of temperature, for compound **1a** (a) and compound **1b** (b).

Table 1 Fitted parameters for the $\chi_M T$ product of compound **1a**

Parameter	Value
g_{tot} [a]	2.041(2)
D	20.0(1) cm^{-1}
Θ	−2.44(4) K

[a] $g_{tot} = (2g_x + g_z)/3$.

$$\chi_x = \frac{N{g_x}^2{\mu_B}^2}{4} \cdot \frac{\frac{9}{k(T-\theta)} + \frac{8}{D} - \frac{11e^{-\frac{2D}{k(T-\theta)}}}{2D} - \frac{5e^{-\frac{6D}{k(T-\theta)}}}{2D}}{1 + e^{-\frac{2D}{k(T-\theta)}} + e^{\frac{-\{6D}{k(T-\theta)}}}.$$

In contrast, complex **1b** shows typical antiferromagnetic behavior with a gradual decline in $\chi_M T$ at low temperatures (Fig. 2b). The Curie–Weiss law describes its magnetic profile well across the full temperature range, consistent with a high-spin Fe^{3+} center. The effective magnetic moment of 5.87(4)μ_B closely matches the spin-only value of 5.91μ_B, with a Curie–Weiss temperature of −7.66 K (Table 2).

These data nicely agree with theoretical computations on gas-phase anions derived from **1a**, **1b**, and **1c**. Indeed, the wavefunction analysis indicates that in all systems the oxidation state of iron is +3, and the most stable spin arrangement presents 5 unpaired electrons in the half-filled *d* shell of the metal atom. The oxidation state of the metal atom remains +3 also considering medium- and low-spin arrangements, where the number of unpaired electrons is 3 and 1, respectively. As for the energetics, medium- and low-spin states are less stable than the high-spin arrangement by more than 10 kcal mol^{-1} in all compounds, and solvation in acetonitrile does not alter this picture (data are collected in Table S10). It is therefore unlikely that thermal energy at 298 K and solvation might induce spin flips or changes in the oxidation state of iron. Based on Mössbauer spectroscopy, macroscopic magnetic measurements, and *ab initio* computations, we can assess that – under the experimental conditions considered in this study – **1a**, **1b**, and **1c** contain an Fe(III) atom with 5 unpaired electrons.

Spectroscopic characterization of the complexes

Fig. 3 reports the experimental and calculated UV-Vis spectra of **1a**, **1b**, and **1c** in acetonitrile; the calculated spectra represent the experimental profile well, except that computed absorptions fall at somewhat different energies with respect to experimental ones, which comes as no surprise considering the limitations of the TD-DFT scheme.[55] Quite importantly, in

Table 2 Results from Curie law and Curie–Weiss law fits for compounds **1a** and **1b**

Sample	μ_{eff} (μ_B, Curie)	μ_{eff} (μ_B, Curie–Weiss)	θ_{CW} (K)
1a	5.5164(4)	5.7063(7)	−5.28
1b	5.7506(2)	5.87(4)	−7.66

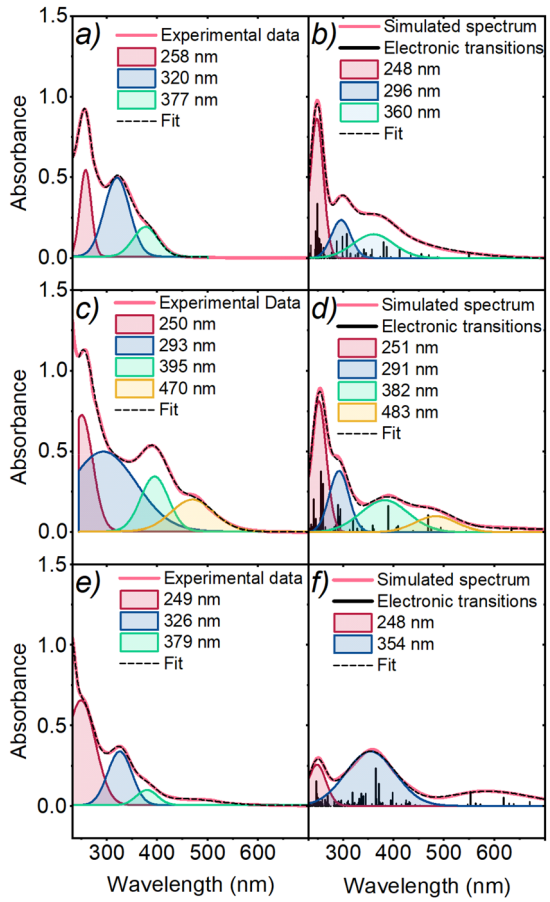

Fig. 3 UV-Vis experimental (left) and theoretical (right) spectra of **1a** (top) (a and b, respectively), **1b** (middle) (c and d), and **1c** (bottom) (e and f) complexes. Left panels: the experimental data are reported as a solid red line, while data obtained by Gaussian fitting are depicted as a dashed black line. Right panels: the computed electronic transitions are reported as solid black lines; the solid red line (the simulated spectrum) is obtained by smearing delta-like absorption peaks with a Gaussian function, and the dashed black line is obtained by fitting the simulated spectrum with the same criterion adopted for experimental data. The fitting Gaussian functions encompass several transitions each, and they are reported as a guide to the eye. In Fig. S10 (SI), all the Gaussians that were used to fit the spectra are reported.

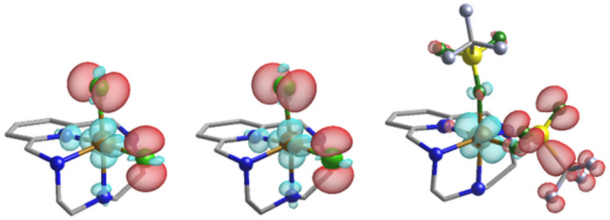

Fig. 4 Representative electron density maps for sample electronic transitions above the dissociation threshold of **1a** (left), **1b** (middle), and **1c** (right). Maps are obtained as the difference between the electron density of the excited state and the ground state, and they refer to the main components of transitions at 357 nm (left), 389 nm (middle), and 486 nm (right). Positive values are in light-blue and negative values are in red. In the three transitions reported, electron excitation removes an electron from the ligands (X) and localizes it onto the Fe atom, which is likely to induce homolytic Fe–X dissociation when this is energetically allowed, *i.e.* in the case of **1a** and **1b**.

the specific systems studied here, the difference between computed and measured spectra allows for a direct comparison between absorption peaks.

The experimental spectrum of **1a** reveals the presence of three main absorption bands centered at 258, 320, and 377 nm. These features are also found in the simulated spectra. As expected, none of the three peaks comes from a single absorption transition. In contrast, they should be ascribed to three clusters of pyclen/Cl ligand-to-metal electronic transitions, which become less intense and more dispersed as the photon energy decreases (see the SI). The inspection of these data revealed the presence of chlorine-to-iron transitions, and the corresponding photon energy resides in the range relevant to the experiments presented here. This prompted us to computationally investigate the possibility of Fe–Cl homolytic bond dissociation. The computed threshold for homolytic breaking of an Fe–Cl bond is 3.34 eV, corresponding to a wavelength of 371 nm, thus falling within the lowest energetic absorption band (green bands in Fig. 3a and b). As can be seen in Fig. 4 (left panel), the wavefunction analysis of the transitions just above the threshold reveals that upon excitation, a single electron is transferred from the chloride ligands to the metal center, and the complex gains enough energy to expel a chlorine radical. Although this is not a rigorous proof that homolytic dissociation occurs, since it does not consider alternative relaxation phenomena and other limiting effects, it is a significant indication that this might be the case, since the excited moiety is higher in energy than the species corresponding to homolytic dissociation.

In **1b**, the less energetic absorption bands are redshifted with respect to **1a**, and they are centered at 395 and 470 nm, respectively (see Fig. 3c). Besides the extension of the absorption towards longer wavelengths, the attribution of the electronic transitions follows similar considerations to what was discussed previously for **1a**. The computed threshold for homolytic dissociation of the Fe–Br bond in **1b** is 2.94 eV (corresponding to 421 nm) and falls between the less energetic electronic transitions (green and orange bands in Fig. 3c and d). In particular, the calculated band centered at 382 nm (green band in Fig. 3d) presents a neat Br-to-metal charge transfer, as shown in Fig. 4 (middle). This intense transition is likely the main reason for the photoinduced homolytic dissociation of an Fe–Br bond in **1b** (*vide infra*).

The experimental spectrum of **1c** is somewhat different from those of **1a** and **1b**. Indeed, it presents two intense bands centered at 249 and 326 nm, followed by a low-intensity broad band centered at 379 nm. The recorded data evidence the presence of another smooth and broad shoulder in the absorbance, located at even longer wavelengths. This feature suggests that several transitions with low intensity are widely distributed around 500 nm. The theoretical simulation of the absorption features of **1c**, indeed, produced two neat peaks at

248 and 354 nm, in agreement with the recorded data. However, their intensities are comparable to each other, while experimentally the peak at 249 nm is much more intense than the one at 326 nm. At longer wavelengths, first principles computations predict a sparse set of transitions, distributed from 550 to 650 nm. This is consistent with the experiment, even if the recorded data are not strictly reproduced by theory. Overall, we can confirm that the allowed electronic transitions of **1c** cover a wider energy range compared to **1a** and **1b**. Most of them have partial ligand-to-metal charge transfer character, and they are almost comparable in intensity to one another, thus generating a poorly structured spectrum. Likely, the difficulty in reproducing the fine details of the experimental spectrum of **1c** reflects the more complex electronic structure of this moiety with respect to **1a** and **1b**, consistent with the reliability of the computational approach adopted.[56] We also note that the predicted geometry of **1c** could not be confirmed by experimental data, at variance with respect to **1a** and **1b**.

Direct calculation of the energy required to promote the homolytic cleavage of the Fe–OTf bond in **1c** was hampered by a proper description of the OTf$^{\bullet}$ radical by DFT (see the SI). We thus estimated a value of 3.89 eV (corresponding to a wavelength of 319 nm), by comparing the relative stability of Cl$^{\bullet}$ and OTf$^{\bullet}$ radicals with the CISD method in terms of the BDFE of H–Cl and H–OTf (CISD stands for Configuration Interaction with Single and Double electron excitations). This high value is in line with the expected instability of the oxygen-centered OTf$^{\bullet}$ radical and rules out the possibility of generating it from **1c** under visible light.

Photochemical aerobic oxidation of *p*-xylene

With the UV-Vis spectroscopy and DFT calculations suggesting the possibility of promoting the homolytic cleavage of the Fe–X bond by light, we finally explored the photochemical activity of iron pyclen complexes towards the light driven aerobic oxidation of organic substrates, in particular *p*-xylene. Among its oxidation products is terephthalic acid, a chemical of interest for the polymer industry with an annual production of *ca.* 90 million tons in 2024 through the Amoco process, employing a cobalt–manganese–bromide catalyst in acetic acid as the solvent, at 175–225 °C temperature and 15–30 bar air pressure.[57–60] Besides terephthalic acid, intermediate oxidation products, such as *p*-methylbenzyl alcohol, *p*-tolualdehyde, and *p*-toluic acid, attract interest. The oxidation of *p*-xylene requires the activation of the benzylic C–H bonds, characterized by a bond dissociation free energy of 80 kcal mol^{-1}; the oxidative activation of C–H bonds is a very hot topic,[61–66] and there is current interest in developing systems for the photochemical oxidation of *p*-xylene exploiting visible light.

Recently, Sun and co-workers used UV irradiation (Hg lamp, 500 W, 0–2 Sun) to boost an ozonization process, reaching 84% terephthalic yield in acetonitrile solvent.[67] The tetrabutylammonium decatungstate photocatalyst was employed in a continuous-flow photoreactor achieving >90% yield of terephthalic acid upon irradiation at 365 nm.[68] The same irradiation wavelength was exploited to activate titanium oxide nanoparticles, for the oxidation of *p*-xylene to *p*-methylbenzyl alcohol and *p*-tolualdehyde as the primary oxidation products.[69] Alternatively, quinone organic photocatalysts, able to promote photochemical hydrogen atom abstraction (hydrogen atom transfer – HAT – reactivity), were considered for the oxidation of *p*-xylene under visible light in acetone solvent, obtaining *p*-toluic acid as the main product, while terephthalic acid was obtained in *ca.* 27% yield from overoxidation of *p*-toluic acid.[70]

As anticipated in the Introduction, inspired by recent reports by Oh and Stache dealing with the photochemical generation of halogen radicals from FeX_3 for the photooxidation of commercial polystyrene,[43] we envisioned investigating the photochemical activity of iron pyclen derivatives. The excitation of ligand-to-metal charge transfer bands in coordination complexes is indeed a convenient strategy for photochemical generation of halogen radicals using low-energy light.[71] Halogen radicals are reactive species for C–H activation,[72] since they can induce HAT reactivity;[73,74] the key reactivity descriptor is the bond dissociation energy of the H–halogen bond, being 102 kcal mol^{-1} for HCl (identifying Cl$^{\bullet}$ as a potent hydrogen atom abstractor), 87 kcal mol^{-1} for HBr and 71 kcal mol^{-1} for HI (I$^{\bullet}$ is indeed not useful for HAT).[75]

We thus tested the photochemical reactivity of **1a–c** towards the oxidation of *p*-xylene (80 mM in acetonitrile solution), using a home-made photoreactor exploiting cheap household lamps emitting white light (33 mW cm^{-2}, equivalent to 1/3 of the irradiation by the sun);[76] see the emission spectrum in Fig. S11 overlapped with absorption spectra of Fe pyclen derivatives. The reaction mixtures from the photocatalytic tests were analyzed through ^{1}H-NMR, adding mesitylene as the internal standard (Fig. S12). The results are summarized in Table 3. The results can be discussed as follows:

(a) **1b** was the only iron complex being significantly active (entries 1–3 in Table 3), promoting the formation of *p*-tolualdehyde as the main reaction product (31 ± 5% yield, corresponding to a turnover of 9.9 ± 1.6 based on the iron catalyst, entry 2 in Table 3). The results were obtained from 6 replicate experiments, including two different batches of **1b**. Control experiments confirmed that light, the iron catalyst, and the aerobic atmosphere are necessary for the photochemical oxidation of *p*-xylene. Running the reaction under an O_2 atmosphere did not lead to a significant improvement of the yield and selectivity (entry 4 in Table 3).

(b) The selectivity for *p*-tolualdehyde among other oxidation products was 79 ± 5%, with *p*-toluic acid also being detected. The C–H bond in aromatic aldehydes is stronger than the C–H bond of a benzylic –CH_3 group (the C–H bond in benzaldehyde has a BDFE of 89 kcal mol^{-1}, while the C–H bond in *p*-xylene has a BDFE of 80 kcal mol^{-1});[63,75] overoxidation of *p*-tolualdehyde is thus more demanding than the oxidation of *p*-xylene and explains the good selectivity of the process.

(c) The reactivity of **1b** is also maintained in acetone as the solvent[43] (entry 5 in Table 3), although with a decreased selectivity (*p*-tolualdehyde yield 20%, selectivity 55%); we also tested the possibility of conducting the reaction in propylene

Table 3 Photocatalytic oxidation of *p*-xylene to *p*-tolualdehyde

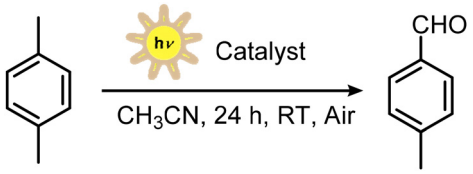

#	Catalyst	Deviations from standard conditions	*p*-Tolualdehyde yield (%)/selectivity (%)	Other products, yield (%)
1	**1a**	—	≈1	—
2	**1b**	—	31 ± 5/79 ± 5	*p*-Toluic acid, 7.5 ± 3 Terephthalic acid, 1.5 ± 0.5 *p*-Methylbenzyl alcohol, <1
3	**1c**	—	5	—
4	**1b**	O_2 instead of air	31/81	*p*-Toluic acid, 6 *p*-Methylbenzyl alcohol, 1
5	**1b**	Acetone as the solvent	20/55	*p*-Toluic acid, 15 *p*-Methylbenzyl alcohol, <1
6	**1b**	Propylene carbonate as the solvent	2/>95	—
7	**1b**	In *p*-xylene neat	—	—
8	$FeCl_3$	—	24 ± 3/56	*p*-Toluic acid, 13 Terephthalic acid, 1 *p*-Methylbenzyl alcohol, 5
9	$FeBr_3$	—	20/66	*p*-Toluic acid, 6 *p*-Methylbenzyl alcohol, 4
10	$FeCl_3$	Acetone as the solvent	4/22	*p*-Toluic acid, 5 Terephthalic acid, 9
11	**1b**	LED 405[a] nm	21/87	*p*-Toluic acid, 1 *p*-Methylbenzyl alcohol, 2

Standard conditions: 1 ml of solution containing 80 mM *p*-xylene and 2.5 mM iron catalyst in acetonitrile, irradiation with white light (33 mW cm^{-2}) for 24 h under an air atmosphere. [a] Irradiation with a blue LED (405 nm, 18 mW cm^{-2}) for 2 hours.

carbonate as a green solvent, where a decreased yield of 2% was registered (entry 6 in Table 3); no reactivity was observed in neat *p*-xylene (entry 7 in Table 3). These results suggest a non-innocent role of the solvent in promoting the target reactivity.

(d) A photochemical reactivity was observed also with $FeCl_3$ and with $FeBr_3$,[43] although with a slightly lower yield with respect to **1b** (entries 8–10 in Table 3). In particular, we observed a decrease in the reaction selectivity and the increased formation of *p*-methylbenzyl alcohol along with *p*-toluic acid as the major by-product.

(e) The reaction with **1b** was accomplished by using a monochromatic LED at 405 nm as the light source, leading to a 21% yield of *p*-tolualdehyde after 2 h (selectivity 87%, entry 11 in Table 3). Estimation of the absorbed photons with a power meter enabled the determination of a quantum yield ϕ_{405} for the production of *p*-tolualdehyde of 0.14%.

All the above indications suggest the photoinduced generation of bromine radicals, which participate in a HAT reaction towards *p*-xylene, forming H–Br and the *p*-xylene radical; this will react with dioxygen to form an organic peroxy free radical that can engage in a HAT reaction with *p*-xylene and feed a chain process (Scheme 2). An EPR analysis in the presence of the 5-*tert*-butoxycarbonyl 5-methyl-1-pyrroline *N*-oxide (BMPO) spin trap[77] revealed the appearance of a multi-component signal compatible with an adduct between BMPO and peroxides as reactive oxygen species,[78,79] although the low intensity of the signal did not allow a reasonable simulation and identification of the components (Fig. S13; BMPO was preferred to DMPO – 5,5-dimethyl-1-pyrrolidine-*N*-oxide – due to its higher stability;[77,78] indeed, very weak EPR signals were observed under the same conditions with the DMPO spin trap). Organic hydroperoxides are characterized by the BDFE of the O–H bond of around 85–90 kcal mol^{-1} (*i.e.* BDFE refers to that of the ROO–H/ROO$^{\bullet}$ couple).[63] The occurrence of a radical based process is also suggested by the kinetic profile of the reaction with **1b**, showing the expected initiation/propagation/termination phases (Fig. S14).

Surprisingly, almost no reactivity was observed for **1a** under analogous conditions: in principle, photochemical homolysis of Fe–Cl in **1a** should lead to the formation of very reactive Cl$^{\bullet}$. The poor reactivity of **1a** may be ascribed to a fast deactivation of the excited state and is currently under further investigation. On the other hand, the high energetic requirement for homolytic bond cleavage of Fe–OTf in **1c** is responsible for the low activity of this complex. We finally verified the stability of the active Fe pyclen complex **1b** under photocatalysis conditions, where UV-Vis analysis revealed minor changes in the absorption spectrum of the compound, suggesting the stability of the Fe(III) pyclen motif (Fig. S15). For comparison, major bleaching of the absorption bands is instead observed for $FeBr_3$ (Fig. S15).

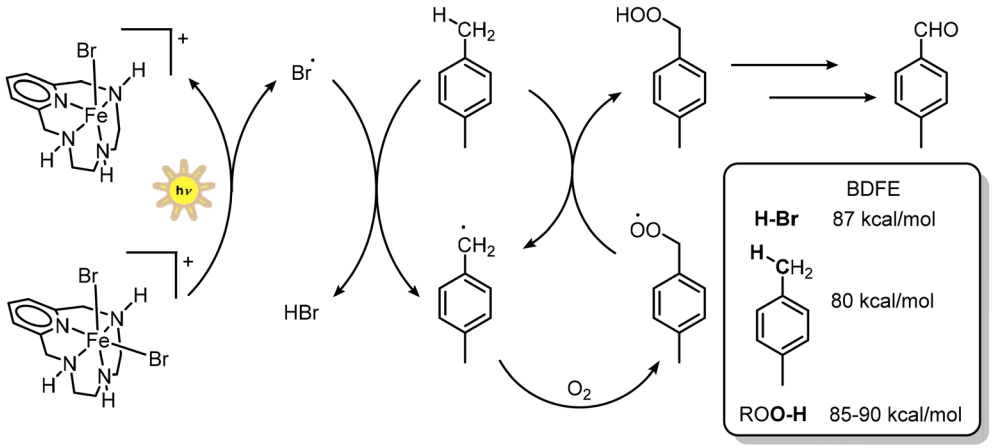

Scheme 2 Proposed photochemical mechanism and competent BDFE values.

Conclusions

In this work, we have reported the synthesis, characterization and photocatalytic reactivity of iron(III) complexes with the tetradentate *N*4 3,6,9-triaza-1(2,6)-pyridinacyclodecaphane ligand (pyclen), [Fe(III)(pyclen)X_2]X (X = Cl, **1a**; X = Br, **1b**; X = OTf, **1c**). In particular, the nature of the counterion has a marked effect on the photocatalytic reactivity of the complexes, enabling the challenging and ambitious light driven aerobic oxidation of *p*-xylene.

The crystal structure of **1a** shows an octahedral Fe(III) center with a *cis*-folded pyclen configuration, with two chloride anions completing the iron coordination sphere, consistent with **1b** and **1c**. Mössbauer and macroscopic magnetic measurements confirmed that the spin state in all the complexes is 5/2, which is consistent with the results that DFT calculations disclosed. The photochemical reactivity of the title complexes was envisaged based on the absorption features in solution, extending up to the visible region and associated with (pyclen/X) ligand-to-iron transitions based on TD-DFT calculations. These absorption features were successfully exploited for the photochemical generation of bromine radicals ($Br^{\bullet}$) from **1b**, responsible for the aerobic oxidation of *p*-xylene to *p*-tolualdehyde under visible light (up to a turnover of 9.9 ± 1.6 for the Fe complex, with a *p*-tolualdehyde selectivity of up to 79 ± 5% among other oxidation products, and a quantum yield of 0.14% at 405 nm).

We believe that this work will contribute to the design of novel photochemical routes exploiting coordination complexes of Earth-abundant transition metals; besides oxidation of substrates of industrial interest like *p*-xylene considered in this work, applications in the photochemical valorization of plastics are appearing in recent literature. Future directions in this field should consider the development of aqueous systems for the valorization of abundant raw materials such as glycerol or furfural derivatives, while possibly red-shifting the use of light towards the visible region.

Author contributions

Matteo Alberti: investigation, data curation, writing – original draft, and visualization. Greta Rossi, Arianna Gentilin, and Luka Đorđević: investigation and data curation. Djihed Boucherabine: data curation and formal analysis. Fausto Cargnoni and Mario Italo Trioni: methodology and theoretical calculations. Giulia Taini: structural determination by single crystal X-ray diffraction and data curation. Dominika Zakutna: writing – review & editing. Andrea Sartorel and Alessandro Caselli: conceptualization, methodology, writing – review & editing, supervision, project administration, and funding acquisition.

Conflicts of interest

There are no conflicts to declare.

Data availability

The data supporting the article have been included as part of the supplementary information (SI). Supplementary information: synthetic procedures, macroscopic magnetization measurements, DFT calculations, single crystal X-ray diffraction analyses, spectroscopic characterization, and catalytic tests. See DOI: https://doi.org/10.1039/d5dt02534f.

The authors have cited additional references (ref. 80–96) within the SI.

CCDC 2404719 contains the supplementary crystallographic data for this paper.[97]

Acknowledgements

We thank the MUR-Italy (PRIN 2022, PROMETEO project 2022KPK8WM and FORCEFUL project 20224KN85Y), the

University of Milan (PSR 2022 – financed project "Catalytic strategies for the synthesis of high added-value molecules from bio-based starting materials" and Ph.D. fellowships to M. A.), and the European Union – Next Generation UE (project "PHOTOCORE" P2022ZSPWF to A. S.) for financial support. Unitech – COSPECT (https://www.cospect.it/), Università degli Studi di Milano, is gratefully acknowledged for HR MS and XRD analyses. DZ acknowledges the assistance provided by the Advanced Multiscale Materials for Key Enabling Technologies project, supported by the Ministry of Education, Youth, and Sports of the Czech Republic Project No. CZ.02.01.01/00/22_008/0004558, co-funded by the European Union. D. Z. was supported by Charles University Research Centre program no. UNCE/24/SCI/010. L.Đ. gratefully thanks the support from the European Union (ERC, PhotoDark, 101077698).

References

1 J. H. E. Teles, I. Ermans, G. Franz and R. A. Sheldon, in *Ullmann's Encyclopedia of Industrial Chemistry*, 2015, pp. 1–103.
2 *Organic Syntheses by Oxidation with Metal Compounds*, ed. W. J. Mijs and C. R. H. I. De Jonge, Plenum, 1986.
3 *Modern Oxidation Methods, 2nd Completely Revised*, ed. J.-E. Bäckvall, Wiley-VCH Verlag GmbH & Co. KGaA, 2010.
4 A. Furstner, Iron Catalysis in Organic Synthesis: A Critical Assessment of What It Takes To Make This Base Metal a Multitasking Champion, *ACS Cent. Sci.*, 2016, **2**, 778–789.
5 I. Bauer and H.-J. Knölker, *Chem. Rev.*, 2015, **115**, 3170–3387.
6 R. J. M. K. Gebbink and M. E. Moret, *Non-Noble Metal Catalysis: Molecular Approaches and Reactions*, Wiley-VCH Verlag GmbH & Co, 2018.
7 S. M. Hoelzl, P. J. Altmann, J. W. Kueck and F. E. Kuehn, *Coord. Chem. Rev.*, 2017, **352**, 517–536.
8 I. Gamba, Z. Codola, J. Lloret-Fillol and M. Costas, *Coord. Chem. Rev.*, 2017, **334**, 2–24.
9 K. Gopalaiah, *Chem. Rev.*, 2013, **113**, 3248–3296.
10 T. Wai-Shan, G. Q. Chen, Y. Liu, C. Y. Zhou and C. M. Che, *Pure Appl. Chem.*, 2012, **84**, 1685–1704.
11 E. P. Talsi and K. P. Bryliakov, *Coord. Chem. Rev.*, 2012, **256**, 1418–1434.
12 M. Costas, *Coord. Chem. Rev.*, 2011, **255**, 2912–2932.
13 S. Enthaler, K. Junge and M. Beller, *Angew. Chem., Int. Ed.*, 2008, **47**, 3317–3321.
14 A. Correa, O. García Mancheño and C. Bolm, *Chem. Soc. Rev.*, 2008, **37**, 1108–1117.
15 W. Nam, *Acc. Chem. Res.*, 2007, **40**, 522–531.
16 E. Rose, B. Andrioletti, S. Zrig and M. Quelquejeu-Etheve, *Chem. Soc. Rev.*, 2005, **34**, 573–583.
17 M. Guo, T. Corona, K. Ray and W. Nam, *ACS Cent. Sci.*, 2019, **5**, 13–28.
18 M. L. Neidig and E. I. Solomon, *Chem. Commun.*, 2005, 5843–5863.
19 L. Vicens and M. Costas, *Dalton Trans.*, 2018, **47**, 1755–1763.
20 O. Cusso, M. W. Giuliano, X. Ribas, S. J. Miller and M. Costas, *Chem. Sci.*, 2017, **8**, 3660–3667.
21 G. Olivo, O. Cusso, M. Borrell and M. Costas, *J. Biol. Inorg. Chem.*, 2017, **22**, 425–452.
22 G. Olivo, O. Cusso and M. Costas, *Chem. – Asian J.*, 2016, **11**, 3148–3158.
23 W. Nam, Y. M. Lee and S. Fukuzumi, *Acc. Chem. Res.*, 2014, **47**, 1146–1154.
24 J. Yoon, S. A. Wilson, Y. K. Jang, M. S. Seo, K. Nehru, B. Hedman, K. O. Hodgson, E. Bill, E. I. Solomon and W. Nam, *Angew. Chem., Int. Ed.*, 2009, **48**, 1257–1260.
25 M. Costas, M. P. Mehn, M. P. Jensen and L. Que Jr., *Chem. Rev.*, 2004, **104**, 939–986.
26 S. H. Bae, X.-X. Li, M. S. Seo, Y.-M. Lee, S. Fukuzumi and W. Nam, *J. Am. Chem. Soc.*, 2019, **141**, 7675–7679.
27 E. Tacchi, E. Anxolabéhère-Mallart, A. Aukauloo, C. Fave, M. Robert and A. Sartorel, *Angew. Chem. Novit.*, 2025, **1**, e70007.
28 W. Nam, *Acc. Chem. Res.*, 2015, **48**, 2415–2423.
29 K. P. Bryliakov and E. P. Talsi, *Coord. Chem. Rev.*, 2014, **276**, 73–96.
30 C.-L. Sun, B.-J. Li and Z.-J. Shi, *Chem. Rev.*, 2011, **111**, 1293–1314.
31 J. Serrano-Plana, W. N. Oloo, L. Acosta-Rueda, K. K. Meier, B. Verdejo, E. García-España, M. G. Basallote, E. Münck, L. Que, A. Company and M. Costas, *J. Am. Chem. Soc.*, 2015, **137**, 15833–15842.
32 J. Serrano-Plana, A. Aguinaco, R. Belda, E. García-España, M. G. Basallote, A. Company and M. Costas, *Angew. Chem., Int. Ed.*, 2016, **55**, 6310–6314.
33 J. Serrano-Plana, F. Acuña-Parés, V. Dantignana, W. N. Oloo, E. Castillo, A. Draksharapu, C. J. Whiteoak, V. Martin-Diaconescu, M. G. Basallote, J. M. Luis, L. Que Jr., M. Costas and A. Company, *Chem. – Eur. J.*, 2018, **24**, 5331–5340.
34 N. Panza, G. Tseberlidis, A. Caselli and R. Vicente, *Dalton Trans.*, 2022, **51**, 10635–10657.
35 G. Tseberlidis, D. Intrieri and A. Caselli, *Eur. J. Inorg. Chem.*, 2017, 3589–3603.
36 G. Tseberlidis, L. Demonti, V. Pirovano, M. Scavini, S. Cappelli, S. Rizzato, R. Vicente and A. Caselli, *ChemCatChem*, 2019, **11**, 4907–4915.
37 N. Panza, A. di Biase, S. Rizzato, E. Gallo, G. Tseberlidis and A. Caselli, *Eur. J. Org. Chem.*, 2020, 6635–6644.
38 A. N. Campbell and S. S. Stahl, *Acc. Chem. Res.*, 2012, **45**, 851–863.
39 S. Fukuzumi and K. Ohkubo, *Chem. Sci.*, 2013, **4**, 561–574.
40 S. Fukuzumi, *Dalton Trans.*, 2015, **44**, 6696–6705.
41 W. J. Zhou, X. D. Wu, M. Miao, Z. H. Wang, L. Chen, S. Y. Shan, G. M. Cao and D. G. Yu, *Chem. – Eur. J.*, 2020, **26**, 15052–15064.
42 S. Bhattacharjee, S. Linley and E. Reisner, *Nat. Rev. Chem.*, 2024, **8**, 87–105.

43 S. Oh and E. E. Stache, *J. Am. Chem. Soc.*, 2022, **144**, 5745–5749.
44 S. Oh and E. E. Stache, *ACS Catal.*, 2023, **13**, 10968–10975.
45 X. Y. Yuan, C. C. Wang and B. Yu, *Chin. Chem. Lett.*, 2024, **35**, 109517.
46 N. W. Alcock, D. H. Busch and C. Y. Liu, CCDC 639154: Experimental Crystal Structure Determination, 2007, DOI: 10.5517/ccpg2w2.
47 M. A. Mekhail, K. Pota, T. M. Schwartz and K. N. Green, *RSC Adv.*, 2020, **10**, 31165–31170.
48 S. M. Brewer, P. M. Palacios, H. M. Johnston, B. S. Pierce and K. N. Green, *Inorg. Chim. Acta*, 2018, **478**, 139–147.
49 S. M. Brewer, K. R. Wilson, D. G. Jones, E. W. Reinheimer, S. J. Archibald, T. J. Prior, M. A. Ayala, A. L. Foster, T. J. Hubin and K. N. Green, *Inorg. Chem.*, 2018, **57**, 8890–8902.
50 S. M. Brewer, T. M. Schwartz, M. A. Mekhail, L. S. Turan, T. J. Prior, T. J. Hubin, B. G. Janesko and K. N. Green, *Organometallics*, 2021, **40**, 2467–2477.
51 N. W. Alcock, D. H. Busch and C. Y. Liu, CCDC 639153: Experimental Crystal Structure Determination, 2007, DOI: 10.5517/ccpg2v1.
52 A. Abedi, N. Safari, V. Amani and H. R. Khavasi, *Dalton Trans.*, 2011, **40**, 6877–6885.
53 V. Felix, J. Costa, R. Delgado, M. G. B. Drew, M. T. Duarte and C. Resende, *J. Chem. Soc., Dalton Trans.*, 2001, 1462–1471.
54 O. Kahn, *Molecular magnetism*, VCH-Verlag, Weinheim, New York, 1993.
55 M. Cazzaniga, F. Cargnoni, M. Penconi, A. Bossi and D. Ceresoli, *J. Chem. Theory Comput.*, 2020, 1188–1199.
56 A. Prlj, B. F. E. Curchod, A. Fabrizio, L. Floryan and C. C. Corminboeuf, *J. Phys. Chem. Lett.*, 2015, **6**, 22.
57 R. A. F. Tomas, J. C. M. Bordado, J. F. P. Gomes and R. J. Sheehan, in *Ullmann's Encyclopedia of Industrial Chemistry*, Wiley–VCH Verlag GmbH & Co. KGaA., 2024.
58 R. A. F. Tomás, J. C. M. Bordado and J. F. P. Gomes, *Chem. Rev.*, 2013, **113**, 7421–7469.
59 N. Aqilah, M. Fadzil, M. Hasbi, A. Rahim and G. P. Maniam, *Chin. J. Catal.*, 2014, **35**, 1641–1652.
60 H. M. Lapa and L. M. D. R. S. Martins, *Molecules*, 2023, **28**, 1922.
61 T. Newhouse and P. S. Baran, *Angew. Chem., Int. Ed.*, 2011, **50**, 3362–3374.
62 Y. Yang, G. A. Volpato, E. Rossin, N. Peruffo, F. Tumbarello, C. Nicoletti, R. Bonetto, L. Paoloni, P. Umari, E. Colusso, L. Dell'Amico, S. Berardi, E. Collini, S. Caramori, S. Agnoli and A. Sartorel, *ChemSusChem*, 2023, e202201980.
63 R. G. Agarwal, S. C. Coste, B. D. Groff, A. M. Heuer, H. Noh, G. A. Parada, C. F. Wise, E. M. Nichols, J. J. Warren and J. M. Mayer, *Chem. Rev.*, 2022, **122**, 1–49.
64 M. Galeotti, M. Salamone and M. Bietti, *Chem. Soc. Rev.*, 2022, **51**, 2171–2223.
65 M. Salamone, M. Galeotti, E. Romero-Montalvo, J. A. Van Santen, B. D. Groff, J. M. Mayer, G. A. Dilabio and M. Bietti, *J. Am. Chem. Soc.*, 2021, **143**, 11759–11776.
66 N. Holmberg-Douglas and D. A. Nicewicz, *Chem. Rev.*, 2022, **122**, 1925–2016.
67 F. Yuan, P. Cao, W. Sun and L. Zhao, *Ind. Eng. Chem. Res.*, 2024, **63**, 82028–88215.
68 Z. Li, Y. Dong, Y. Zeng, M. Zhang, H. Lv and G. Y. Yang, *Chin. J. Catal.*, 2024, **66**, 282–291.
69 X. Sun, Z. Feng, S. Wang, Q. N. Wang, P. Zhang, R. Li and C. Li, *ACS Catal.*, 2024, **14**, 5356–5365.
70 D. Jiang, Q. Zhang, L. Yang, Y. Deng, B. Yang, Y. Liu and C. Zhang, *Renewable Energy*, 2021, **174**, 928–938.
71 S. M. Treacy and T. Rovis, *J. Am. Chem. Soc.*, 2021, **143**, 2729–2735.
72 Q. Yang, Y. Wang, Y. Qiao, M. Gau, P. J. Carroll, P. J. Walsh and E. J. Schelter, *Science*, 2021, **372**, 847–852.
73 E. Skolia, O. G. Mountanea and C. G. Kokotos, *ChemSusChem*, 2024, e202400174.
74 S. Rohe, A. O. Morris, T. McCallum and L. Barriault, *Angew. Chem., Int. Ed.*, 2018, **57**, 15664–15669.
75 B. Saxena, R. I. Patel and A. Sharma, *RSC Sustainability*, 2024, **2**, 2169–2189.
76 Y. Yang, M. Nalesso, A. Basagni, R. Bonetto, R. Signorini, S. Agnoli, L. Đorđević and A. Sartorel, *J. Mater. Chem. A*, 2025, **13**, 18436–18444.
77 H. Zhao, J. Joseph, H. Zhang, H. Karoui and B. Kalyanaraman, *Free Radicals Biol. Med.*, 2001, **31**, 599–606.
78 S. S. Ranade, D. F. Zamudio Díaz, M. C. Meinke and S. B. Lohan, *Chem.-Biol. Interact.*, 2025, **421**, 111744.
79 L. Gerritz, J. Wei, T. Fang, C. Wong, A. L. Klodt, S. A. Nizkorodov and M. Shiraiwa, *Environ. Sci. Technol.*, 2024, **58**, 4716–4726.
80 M. Trose, M. Dell'Acqua, T. Pedrazzini, V. Pirovano, E. Gallo, E. Rossi, A. Caselli and G. Abbiati, *J. Org. Chem.*, 2014, **79**, 7311–7320.
81 J. S. Haynes, J. R. Sams and R. C. Thompson, *Can. J. Chem.*, 1981, **59**, 647–758.
82 CrysAlis PRO, *CrysAlisPRO*, Oxford Diffraction/Agilent Technologies UK Ltd, Yarnton, England, 2019.
83 G. Sheldrick, *Acta Crystallogr., Sect. A:Found. Adv.*, 2015, **71**, 3–8.
84 L. J. Farrugia, *J. Appl. Crystallogr.*, 2012, **45**, 849–854.
85 M. Swart, A. R. Groenhof, A. W. Ehlers and K. Lammertsma, *J. Phys. Chem. A*, 2004, 5479–5483.
86 M. Swart, A. W. Ehlers and K. Lammertsma, *Mol. Phys.*, 2004, **102**, 2467–2474.
87 A. V. Marenich, C. J. Cramer and D. G. Truhlar, *J. Phys. Chem. B*, 2009, **113**, 6378–6396.
88 M. M. Flores-Leonar, R. Moreno-Esparza, V. M. Ugalde-Saldívar and C. Amador-Bedolla, *ChemistrySelect*, 2017, **2**, 4717–4724.
89 E. A. Bleda, C. Trindle and Z. Altun, *Comput. Theor. Chem.*, 2015, **1073**, 139–148.
90 O. S. Siig and K. P. Kepp, *J. Phys. Chem. A*, 2018, **122**, 4208–4217.
91 G. Brauer, *Handbook of preparative inorganic chemistry*, Academic press, 2nd edn, 1963, vol. 1.

92 M. Nardelli, *J. Appl. Crystallogr.*, 1995, **28**, 659–659.
93 B. Bosnich, C. K. Poon and M. L. Tobe, *Inorg. Chem.*, 1965, **4**, 1102–1108.
94 R. Ketkaew, Y. Tantirungrotechai, P. Harding, G. Chastanet, P. Guionneau, M. Marchivie and D. J. Harding, *Dalton Trans.*, 2021, **50**, 1086–1096.
95 J. M. Holland, J. A. Mcallister, Z. Lu, C. A. Kilner, M. Thornton-Pett and M. A. Halcrow, *Chem. Commun.*, 2001, 577–578.
96 J. Elhaïk, C. A. Kilner and M. A. Halcrow, *CrystEngComm*, 2005, **7**, 151–157.
97 CCDC 2404719: Experimental Crystal Structure Determination, 2025, DOI: 10.5517/ccdc.csd.cc2lq9l7.